

Article

The PIV Measurements of Time-Averaged Parameters of the Synthetic Jet for Different Orifice Shapes

Emil Smyk ^{1,*} , Paweł Gil ² , Petra Dančová ³ and Miroslav Jopek ⁴

¹ Faculty of Mechanical Engineering, Bydgoszcz University of Science and Technology, Al. Prof. S. Kaliskiego 7, 85-796 Bydgoszcz, Poland

² Faculty of Mechanical Engineering and Aeronautics, Rzeszow University of Technology, al. Powstańców Warszawy 12, 35-959 Rzeszów, Poland

³ Department of Power Engineering Equipment, Faculty of Mechanical Engineering, Technical University of Liberec, Studentska 2, 461 17 Liberec, Czech Republic

⁴ Department of Metal Forming and Plastic, Faculty of Mechanical Engineering, Brno University of Technology, Technická 2, 616 69 Brno, Czech Republic

* Correspondence: emil.smyk@pbs.edu.pl

Featured Application: Velocity and turbulence analysis provides the information needed when designing actuators for heat transfer, active jet control, or mixing applications.

Abstract: In the present study, the flow fields generated by a synthetic jet (SJ) were investigated with particle image velocimetry (PIV). The SJ time-averaged parameters, such as velocity, turbulent kinetic energy (TKE), and vorticity, were compared by using the Reynolds number ($Re = 5000$) and dimensionless stroke length ($L_0 = 2; 10$). Three different orifice shapes with the same equivalent diameter were used: circle, square, and slot. The flow fields of the investigated parameters were presented and discussed at a distance from the orifice $x/d \leq 10$, and the difference in radial and axial profiles were compared. The impact of the orifice shape and dimensionless stroke length on the investigated parameters was discussed.

Keywords: ZNMF; vorticity; turbulent; TKE; PIV



Citation: Smyk, E.; Gil, P.; Dančová, P.; Jopek, M. The PIV Measurements of Time-Averaged Parameters of the Synthetic Jet for Different Orifice Shapes. *Appl. Sci.* **2023**, *13*, 328. <https://doi.org/10.3390/app13010328>

Academic Editors: Richard Lenhard, Jozef Jandačka and Ladislav Dzurenda

Received: 18 November 2022

Revised: 13 December 2022

Accepted: 22 December 2022

Published: 27 December 2022



Copyright: © 2022 by the authors. Licensee MDPI, Basel, Switzerland. This article is an open access article distributed under the terms and conditions of the Creative Commons Attribution (CC BY) license (<https://creativecommons.org/licenses/by/4.0/>).

1. Introduction

The synthetic jet (SJ) has been investigated since the 1950s and still has attracted the attention of numerous researchers due to its many potential applications, such as enhanced heat transfer [1,2], flow control [3,4], and mixing [5,6]. SJ is generated by periodic expulsion and injection of some volume of fluid through an orifice or a nozzle. The time-mean mass flow rate in the orifice cross-section is equal to zero; therefore, the SJA is called a zero-net mass-flux device (ZNMF). However, at some axial distance from the orifice, the vortex ring is generated. The change in the volume of the cavity of the synthetic jet actuator (SJA) is performed by replacing one or more cavity walls with a movable or deformable element such as a piezoelectric [7,8], a loudspeaker [9,10], or piston [11,12]. Plasma SJA is additionally distinguished [13].

The two fundamental experimental methods of SJ flow field investigation are hot-wire anemometry (HWA) and particle image velocimetry (PIV). Although the HWA allows measurements of the flow only in one or more points (depending on the number of probes), the PIV measures the velocity in a plane or volume. There is a good agreement between PIV and HWA measurements, but PIV has a larger uncertainty than HWA [13]. Depending on the type of the PIV system, the noise level should be even three times lower than the noise level in HWA. Smith and Glezer [14] used the HWA and schlieren visualization in the investigation of the slot SJ. Carter and Soria [15] were among the first to use the PIV method in the SJ investigation. They measured the vorticity and velocity of the SJ and

continuous jet at a far distance from the orifice ($0 < x/d < 30$, where x is the distance from the orifice (m) and d is the diameter of the orifice (m)) and pointed to the similarity between the continuous jet and SJ at a high Reynolds number and low Strouhal number or high distance, x/d , respectively. In the next part of the Introduction, we focus on the investigations performed using the PIV method.

Violato and Scarano [16] investigated the evolution of circular and chevron SJ at a constant Reynolds number ($Re = 5000$). They described the phenomenon of vortex merging, which results in azimuthal disturbances in the vortex ring, and the phenomenon of the formation of longitudinal pairs of vortex structures in the case of circular SJ. The topology of the chevron SJ was more complicated, and the coherence of the axisymmetric ring was replaced by streamwise flow structures by Crispio et al. [17]. Crispio et al. [17] showed that the turbulent kinetic energy (TKE) increased near the nozzle in the case of the chevron orifice and the TKE decreased at a distance of $1.5 < x/d < 4.5$. Shuster and Smith [18] used the slug parameters and proved that SJ can be distinguished by two dimensionless parameters: dimensionless stroke length (L_0) and Reynolds number (Re). The dimensionless stroke length equal to 1 was determined as an SJ formation criterion, whereas Holman et al. [19] determined the axisymmetric SJ formation criterion to be $L_0 = 0.5$. Shuster and Smith [18] described the evolution of SJ and described the values of the Reynolds number and orifice distance (x/d) for which the formed vortex ring is laminar, transitional, or turbulent.

Miró et al. [20] investigated circular and slot SJ for enhanced heat transfer at low Reynolds numbers (50, 300, and 500). The slot SJ characterized the higher TKE and also the lack of coherent structure of the vortex. For this reason, the slot SJ provides a better cooling performance than the circular SJ, especially at a small distance from the orifice. This observation was also pointed out in [21,22]. However, Chaudhari et al. [22] found that for a far distance from the orifice ($x/d > 5$), the square SJ is better than the slot SJ.

The visualization of the circular, slot, and square SJ was performed by Wang et al. [12]. The similarity between square and circular SJs was indicated. However, the square SJ had azimuthal deformation in a plane corresponding to the diagonal of the orifice cross-sectional area. Wang et al. [12] did not observe longitudinal stream-wise vortices for the square and circle SJ, which were observed by Violato and Scarano [16]. These structures were observed for the slot SJ at an aspect ratio of $AR = 5$ ($AR = b/a$, where a is the length of the shorter side of the orifice (m), and b is the length of the longer side of the orifice (m)). Wang et al. [12] observed the vortex bifurcation at $AR = 5$.

The impinging SJ configuration is commonly used in the cooling application, and this is the reason for investigating its flow fields. Ghaffari et al. [23] investigated the slot, impinging SJ. They noted the importance of the Stokes number. The PIV visualization of the SJ showed that the SJ at the same Reynolds number may have markedly different flow responses depending on the Stokes number. They also noticed the reduction of heat transfer for small orifice-to-surface distances due to the reduced space for the growth of the vortex ring. Ghaffari et al. [23] observed the additional vortex ring that separated from the main vortex after impinging into the wall. The same observation was made by Xu and Wang [11] but only at a high dimensionless stroke length ($L_0 = 7.2$). At smaller dimensionless stroke lengths, the vortex rings accumulated and formed a large-scale vortical structure in the near-wall region. The PIV measurements of the SJ in heat-transfer-enhancement application were made also by Zhao et al. [24], Miró et al. [20], and others [6,25].

In this study, the PIV was used in the investigation of the free SJ flow field. The time-averaged flow parameters for the circle, square, and slot orifice were determined. The SJA with orifices used in this paper was earlier investigated by Smyk et al. [26]. They used a time-mean reaction force method described by Gil [27] and HWA. The investigation presented in this paper was the follow-up of the research presented in [26]. The cross-sectional area and equivalent diameter are the same for each orifice. The time-averaged velocity, the TKE, and the vorticity of the SJ at the same Reynolds number and two different dimensionless stroke lengths were investigated in this study.

2. Methods

The circle, slot, and square orifices printed with PETG (polyethylene terephthalate glycol-modified) were fastened in the PMMA actuator body (Figure 1). The thickness of the orifice wall was 2 mm. The characteristic parameters of the SJ orifices are presented in Table 1. The diameter of the actuator cavity was 150 mm, and the height was 20 mm. The STX M.18.200.8.MCX loudspeaker with a nominal impedance equal to 8Ω , sensitivity ($2.83 \text{ V}/1 \text{ m}$) equal to 89 dB, and a nominal resonance frequency equal to 37 Hz was used as an actuator in the SJA. The same actuator body, loudspeaker, and orifices were used in [26], where the characteristic frequency of the SJA was designated as $f = 44 \text{ Hz}$ in the case of the circle and the square orifice and $f = 54 \text{ Hz}$ in the case of the slot orifice.

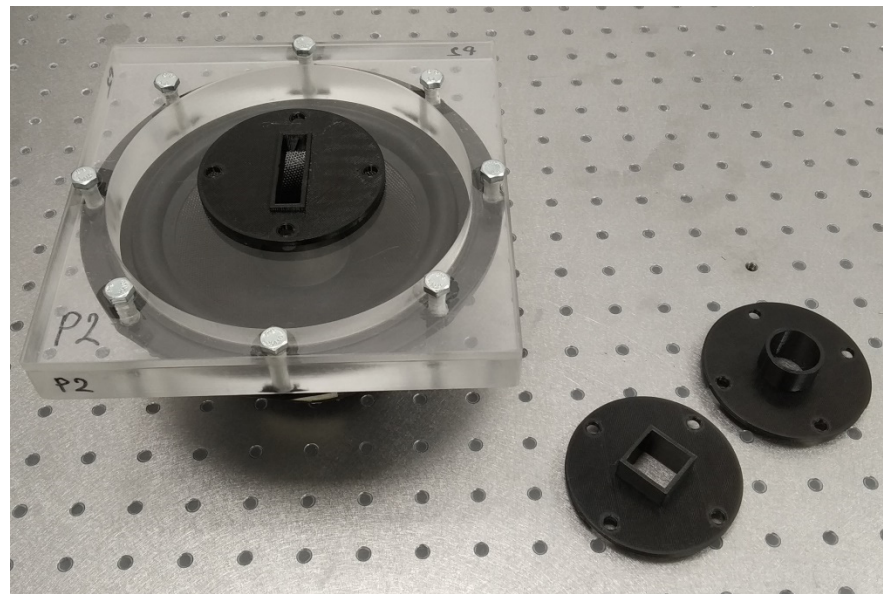


Figure 1. Synthetic jet actuator with various orifice shapes: circle, square, and slot.

Table 1. Geometric and operation parameters of SJA.

Orifice	Dimension (mm)	A (mm ²)	d (mm)	U_e (m/s)	f (Hz)	Re	L_0	St
Circle	$d = 22.4$	394	22.4	3.37	75	5000	2	0.5
				3.37	15	5000	10	0.1
Square	$a = b = 20$	400	22.57	3.35	74	5000	2	0.5
				3.35	14.8	5000	10	0.1
Slot	$a = 10, b = 40$	400	22.57	3.35	74	5000	2	0.5
				3.35	14.8	5000	10	0.1

The ratio $d/D = 0.17$ (where d is the equivalent diameter of the actuator orifice (mm), and $D = 130$ is the diameter of the effective area of the loudspeaker (mm)) was used to calculate the diameter of the circle orifice. The value $d/D = 0.17$ is in the range for which Kordík and Trávníček [28] found the optimal diameter for the SJ actuator.

The actuator was supplied with a sinusoidal signal from the signal generator GWINSTEK AFG-2225 and amplified by an EMOTIVA A2 amplifier. The true-RMS current and voltage were measured with GWINSTEK GDM-8351.

Instantaneous SJ velocity fields were measured by using PIV from Dantec Dynamics. The laser sheet was generated with the Litron Bernoulli series laser system with two pulsed and Q-switched Nd: YAG laser resonators, producing visible green 532 nm laser light. The laser had a maximum output energy equal to 200 mJ per pulse and a repetition rate equal to 15 Hz. The thickness of the laser sheet was approximately 1 mm. The laser sheet covers the camera field of view and passes through the orifice radial coordinate presented

in Figure 2; the axial coordinate, x , passes through the orifice centerline and starts at the orifice exit plane. The images were acquired with an Imperx B3440 CCD camera with a sensor resolution of 3388×2712 pixels at 17 fps, and each pixel depth equals 12 bits. The camera used a lens with a 50 mm focal length, and the aperture was set to 1.8. The field of view is equal to $256 \text{ mm} \times 205 \text{ mm}$; thus, the resulting resolution for the digital image is 13.2 pixels/mm. A component of the PIV system was synchronized with the use of the Dantec Dynamics High-Performance Synchronizer with 32 independent outputs. The air was seeded with DEHS oil droplets with a nominal diameter of approximately $2 \mu\text{m}$. The SJA was closed in a $1000 \times 500 \times 500 \text{ mm}$ transparent box to prevent the spread of DEHS and to ensure adequate seeding concentration in the measuring area. Measurements were performed on the STANDA optical table equipped with vibration dampers. The entire test stand and its components are shown in Figure 3.

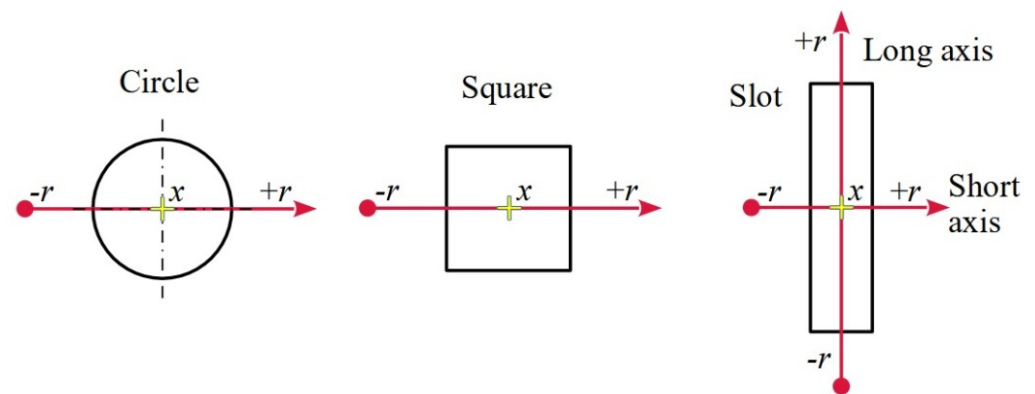


Figure 2. The coordinate system for various orifice shapes. The longitudinal direction is perpendicular to the page.

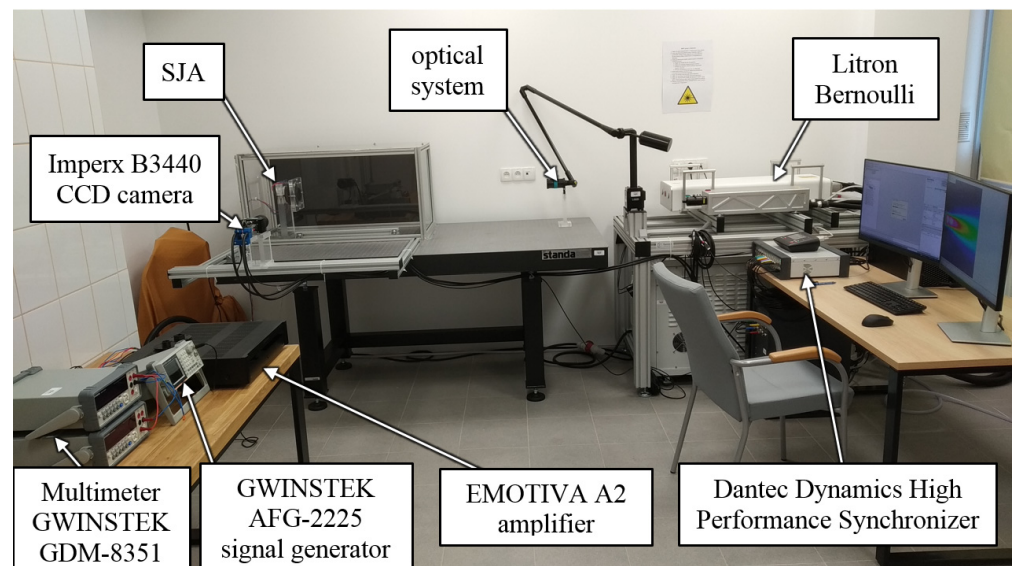


Figure 3. Experimental setup.

The adaptive PIV algorithm was used to calculate velocity vectors, and the interrogation area was automatically chosen between the 32×32 and 64×64 pixel range. The final vector map has 210×168 vectors, which correspond to the spatial resolution of a single vector equal to $1.22 \times 1.22 \text{ mm}$. A validation algorithm was applied for the rejection of the outlier vector, and the relative value of the rejected vector was less than 3%. The PIV uncertainty algorithm was applied to the acquired data according to the method based on the peak height ratio [29]; the relative value of the expanded uncertainty at the level of

confidence of 95% is typically less than 3% of the measured value. The PIV sampling is limited to 8.5 Hz, while the SJA operates up to 75 Hz; thus, the PIV sampling frequency was calculated according to the equation provided by Greco et al. [30]:

$$f_{PIV} = \frac{f}{\frac{1}{N_{div}} + n} \quad (1)$$

where f is an operating frequency of an actuator (Hz), N_{div} is the number of the phases which are sampled, and n is the number of the membrane oscillation period. The acquisition was carried out by sampling the phenomenon every period of the SJA periods with a phase shift of $360^\circ/N_{div}$ (where $N_{div} = 360$ is the number of phases); thus, the SJ was sampled every 1° . The acquisition includes 1440 double-frame images for calculating the time-averaged flow field.

2.1. Data Reduction

The SJ parameters during investigations were measured by the same Reynolds number, which may be defined as follows:

$$Re = \frac{d \cdot U_e}{\nu} \quad (2)$$

where d is the equivalent diameter of the actuator orifice (mm), ν is a kinematic viscosity of operation fluid (m^2/s), and U_e is a characteristic velocity of SJ. The characteristic velocity is defined as follows:

$$U_e = \frac{1}{TA} \int_A \int_0^{T/2} u d\tau dA \quad (3)$$

where T is an oscillation period of loudspeaker membrane (s), A is an orifice cross-section area (mm^2), u is the instantaneous velocity in the x -direction (m/s), and τ is the time (s).

The equivalent diameter of the actuator orifice was calculated as follows [26]:

$$d = \sqrt{4 \frac{A}{\pi}} \quad (4)$$

The Strouhal number based upon the equivalent diameter; oscillation frequency, f , (Hz); and characteristic velocity is given by the following equation [15,31]:

$$St = \frac{f \cdot d}{U_e} \quad (5)$$

The dimensionless stroke length was calculated as follows [11,32]:

$$L_0 = \frac{U_e}{df} \quad (6)$$

The Strouhal number and the dimensionless stroke length are the variables that are commonly used to describe the SJ. The Strouhal number is the reverse of the dimensionless stroke length; therefore, they can be used alternately.

The characteristic velocity, U_e , was calculated from the reaction force measurement on the precision balance. The force measurement technique is described in detail in [32], while the relationship between the characteristic velocity (U_e) and reaction force was adapted from [33] in the following form:

$$U_e = F \frac{2}{\pi} \sqrt{\frac{4mg}{\rho \pi d^2}} \quad (7)$$

where m is a mass measured by balance (kg), g is the gravitation acceleration (m/s^2), ρ is the air density (kg/m^3), and F is a correction factor equal to the following [33]:

$$F = \begin{cases} 0.5 \leq L_0 < 5 \Rightarrow 1.22L_0^{-0.1} \\ 5 \leq L_0 \leq 68 \Rightarrow 1.02 \end{cases} \quad (8)$$

The other parameters used in the paper are the time-averaged velocity in the x - and r -direction and their variances, which were calculated as follows:

$$U = \frac{1}{N} \sum u \quad (9)$$

$$V = \frac{1}{N} \sum v \quad (10)$$

$$\sigma_u^2 = \frac{1}{N-1} \sum (u - U)^2 \quad (11)$$

$$\sigma_v^2 = \frac{1}{N-1} \sum (v - V)^2 \quad (12)$$

where N is the number of measurements, and v is instantaneous velocity in the r -direction (m/s). Based on these variables, the turbulent kinetic energy (TKE) and the local vorticity in a plane (x, r) were computed as follows:

$$TKE = \frac{3}{4} (\sigma_u^2 + \sigma_v^2) \quad (13)$$

$$\omega = \frac{\partial V}{\partial x} - \frac{\partial U}{\partial r} \quad (14)$$

2.2. Validation of PIV Measurement

The validation consists of the comparison of the centerline synthetic jet time-averaged velocity with the PIV and hot-wire measurement methods. The eight-channel ATU-08 hot-wire anemometer was used for velocity measurements (see [26]). The probe was calibrated in the range of 0.1–50 m/s , with an accuracy of $\pm 0.05 \text{ m/s}$ in the velocity range of 0.1–2.6 m/s and $\pm 0.14 \text{ m/s}$ for a velocity greater than 2.6 m/s .

Based on Figure 4, it should be considered that the PIV measurements were carried out correctly. The convergence between PIV and hot-wire measurements was complete.

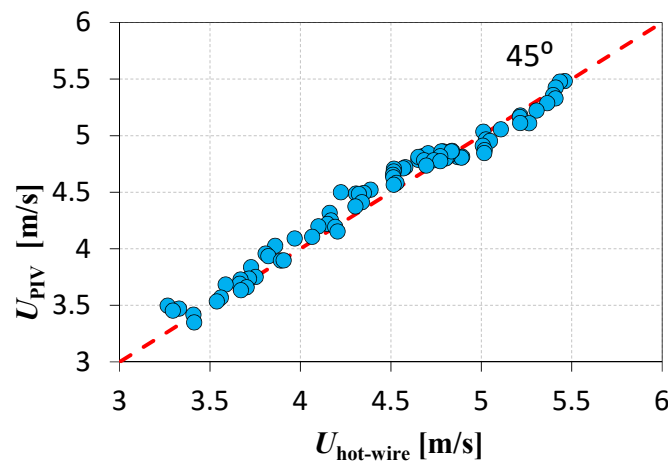


Figure 4. The comparison of the synthetic jet centerline time-averaged velocity obtained with PIV and hot-wire at $Re = 5000$, $St = 0.5$, and $L_0 = 2$. Circular orifice.

3. Results and Discussion

This part of the paper is divided into four sections. In the first three sections, dimensionless velocity, turbulent kinetic energy, and vorticity are presented and discussed for the circle, square, and slot orifice SJA, respectively, in Sections 3.1–3.3. Each of these sections is divided into two subsections: the first discusses the impact of the orifice shape on the discussed parameter, and the second discusses the impact of the dimensionless stroke length on the discussed parameter.

3.1. The Velocity of the Synthetic Jet

In Figures 5 and 6, the dimensionless time-averaged velocity fields at $Re = 5000$ and $L_0 = 2$ and 10 were presented, respectively. The velocity fields for the circle and square orifices are similar at the same dimensionless stroke length. In the case of the slot orifice, there are significant differences along the long- and short-axis velocity fields compared to the circle and square orifices. It must be noted that the characteristic velocity, U_e , of SJ was the same in each case (Table 1). The change of the dimensionless stroke length, L_0 , was realized by the change of the SJ operation frequency and the real power of the supply. The velocity component discussed in the present section was the time-averaged velocity in the x -direction.

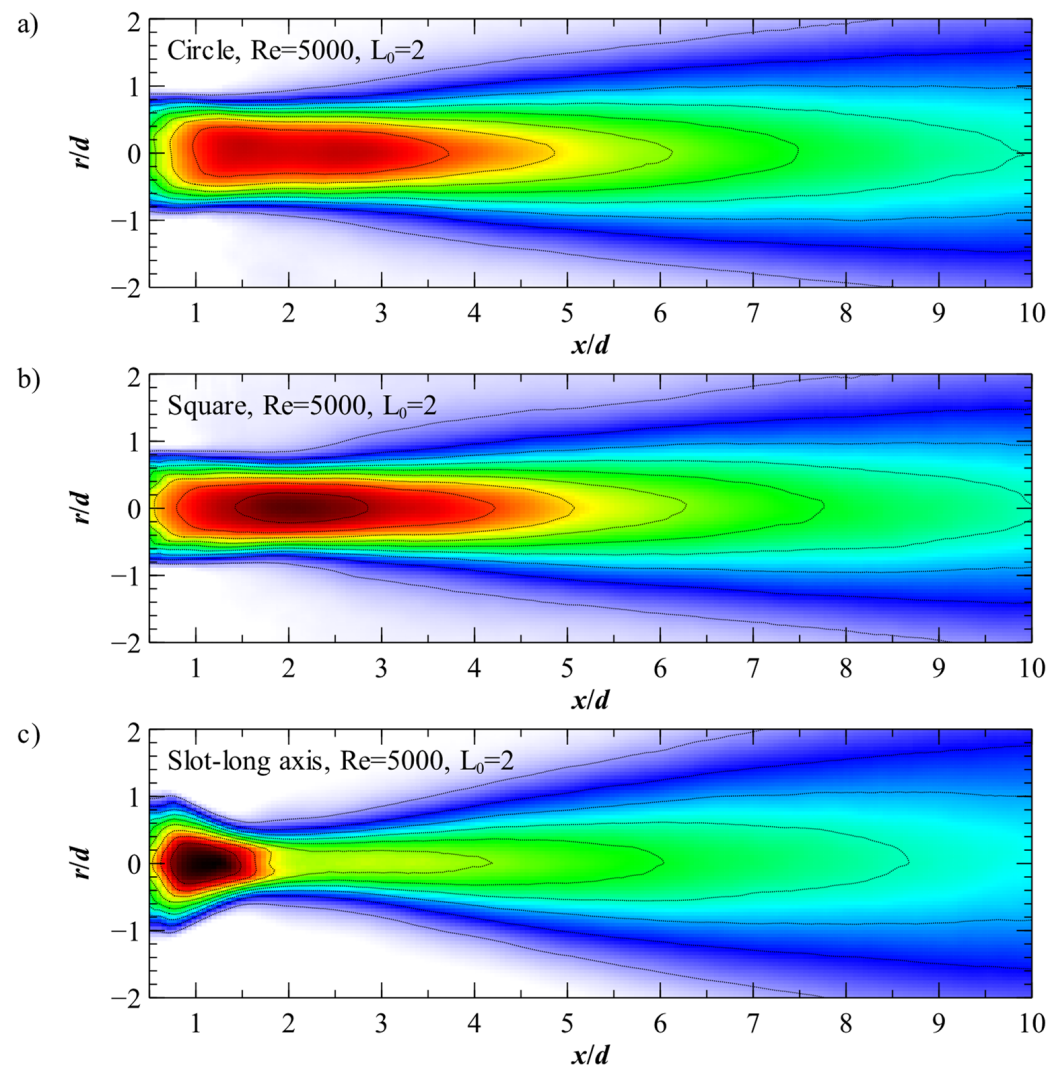


Figure 5. Cont.

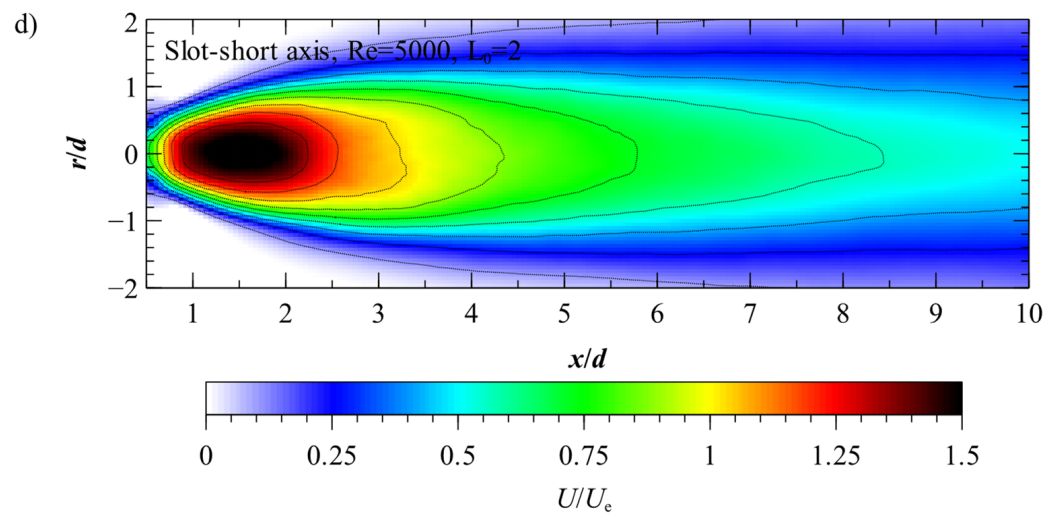


Figure 5. Synthetic jet dimensionless time-averaged velocity field at $Re = 5000$, $St = 0.5$, and $L_0 = 2$: (a) circle orifice, (b) square orifice, (c) slot-long side, and (d) slot-short side.

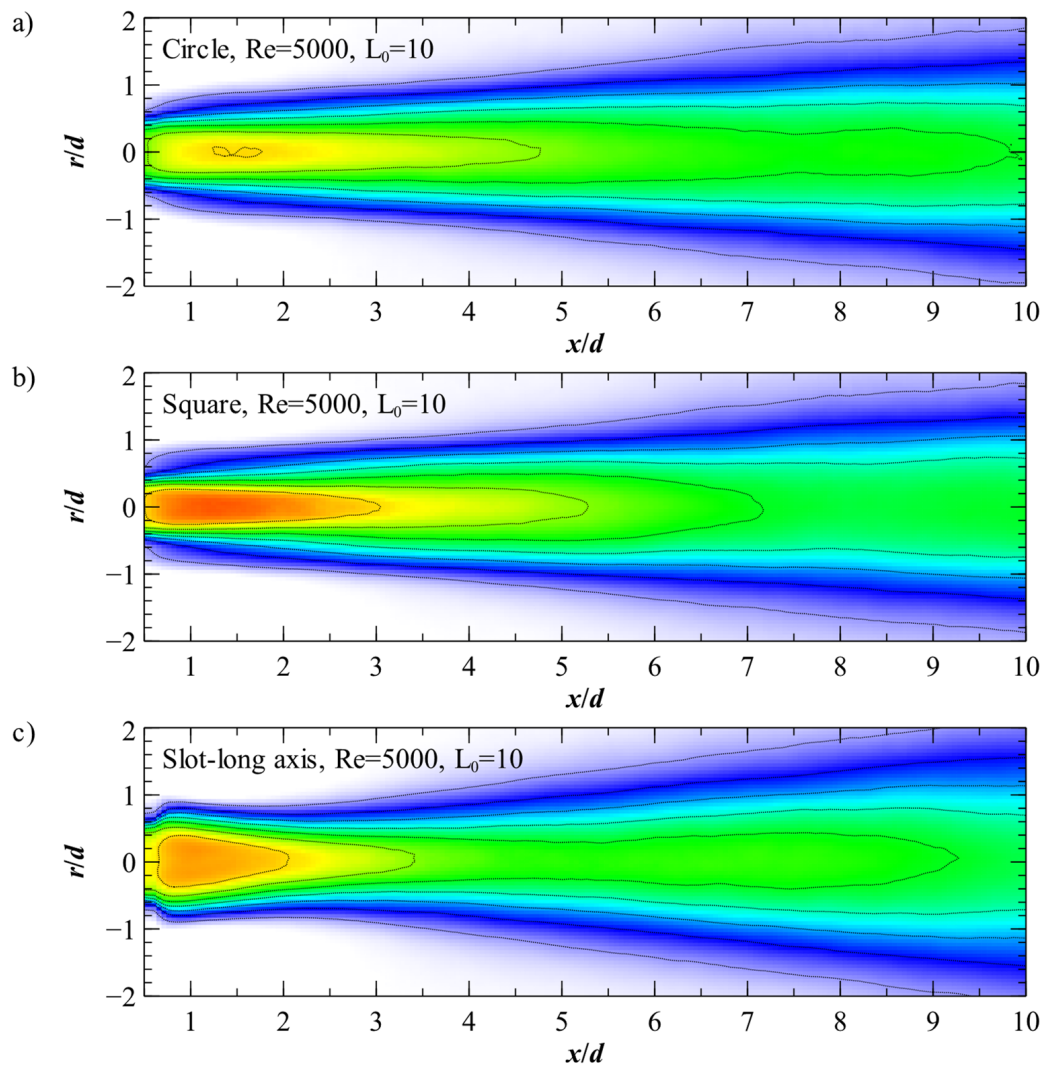


Figure 6. Cont.

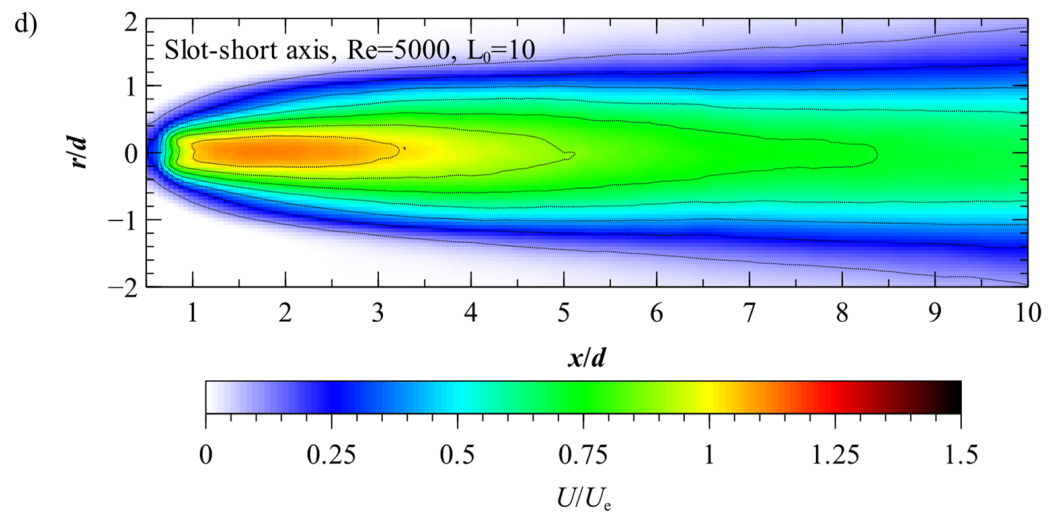


Figure 6. Synthetic jet dimensionless time-averaged velocity field at $Re = 5000$, $St = 0.1$, and $L_0 = 10$: (a) circle orifice, (b) square orifice, (c) slot-long side, and (d) slot-short side.

In Figures 7 and 8, the axial distributions of the centerline dimensionless time-averaged velocity were presented at $Re = 5000$ and $L_0 = 2$ and 10 , respectively, while in Figures 9 and 10, the radial distributions of the centerline dimensionless time-averaged velocity were presented.

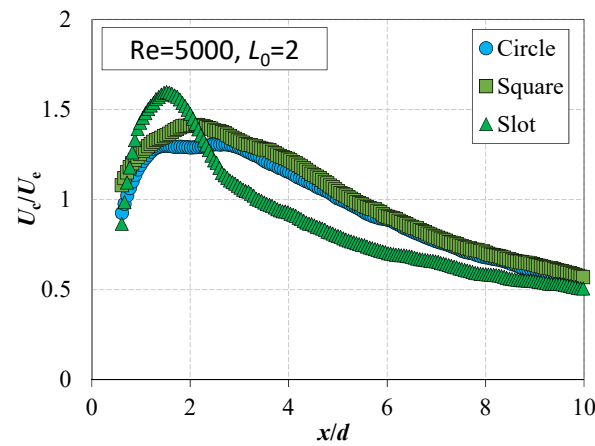


Figure 7. Centerline dimensionless time-averaged velocity axial distribution at $L_0 = 2$.

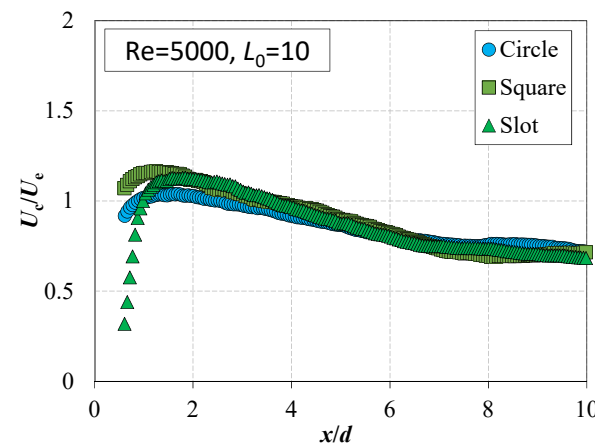


Figure 8. Centerline dimensionless time-averaged velocity axial distribution at $L_0 = 10$.

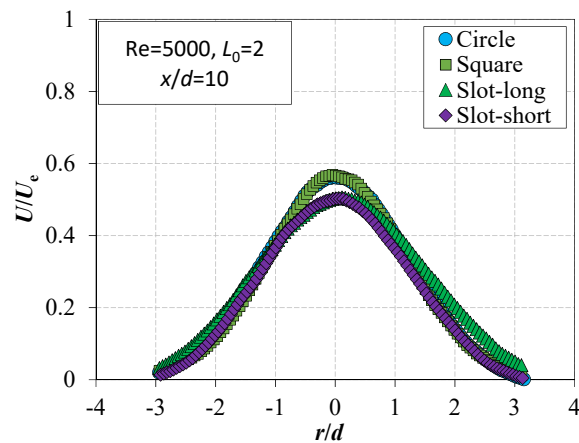


Figure 9. Dimensionless time-averaged velocity radial distribution at $L_0 = 2$.

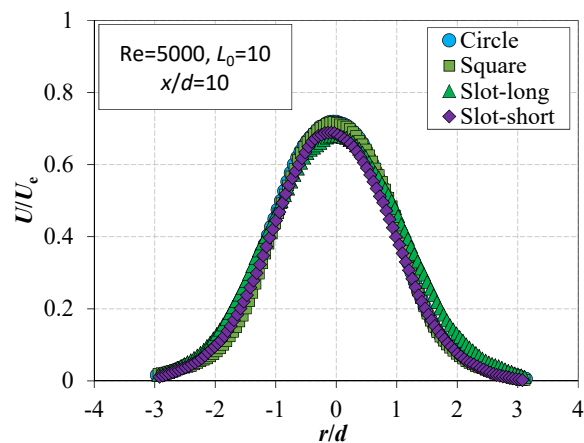


Figure 10. Dimensionless time-averaged velocity radial distribution at $L_0 = 10$.

3.1.1. Impact of the Orifice Shape on the Velocity

For the circle orifice, the time-averaged dimensionless velocity was the highest in the range of $1 < x/d < 3.5$ at $L_0 = 2$ (Figure 5a), and in the range of $1 < x/d < 2.5$ at $L_0 = 10$ (Figure 6a). The SJ expands at the axial and radial directions, but the rate of expansion was higher for a lower dimensionless stroke length (compare Figures 4 and 5). The time-averaged velocity in the vicinity of the orifice tends toward zero due to the fact that the SJA is called the zero-net-mass-flux; similar results were presented in Refs. [23,24]. The velocity fields for the circle and square orifice are very similar for both values of dimensionless stroke length. The time-averaged SJ velocity field for the circle orifice for $x/d < 2$ was very similar to the time-averaged velocity field determined for continuous jet by Antošov and Trávníček [34] at $Re = 5181$; the similarity between the continuous jet and the SJ was confirmed many times [3,35,36].

The dimensionless time-averaged velocity field for the slot orifice is completely different than it is for the circle and square orifices. In the case of the slot-long axis (Figures 5c and 6c), the SJ velocity field in the radial direction contracts at a distance of $0.5 < x/d < 2$. In the case of the slot-short axis (Figures 5d and 6), rapid radial expansion is observed. The same phenomenon for the slot orifice was observed by Zhong and Kotsonis [37] and Zhao et al. [24].

The centerline distributions of the time-averaged velocity were presented in Figures 7 and 8. The SJ velocity value tends toward zero near the orifice area, $x/d = 0$. It can be assumed that the result obtained near the orifice ($x/d < 0.5$) was burdened with an additional error, due to the proximity of the orifice. This is especially visible for the slot-short side dimensionless time-averaged velocity field (Figures 5d and 6d). In this case, the orifice edge

was the smallest (Table 1, $a = 10$), and therefore the impact of the orifice on the movement of the particles was the highest.

The centerline dimensionless time-averaged velocity was higher in the case of a square orifice than in the case of a circle orifice at a distance $x/d < 6$. The centerline velocity in the case of the slot orifice was the highest at $L_0 = 2$ and $x/d = 1.8$, but already at a distance of $x/d = 2$, it decreased below the value obtained for the circle and square orifice. The centerline time-averaged SJ velocity for a dimensionless stroke length equal to 10 has similar values and distributions for all investigated orifices for $x/d > 1$.

3.1.2. Impact of the Dimensionless Stroke Length on the Velocity

The increase in the dimensionless stroke length had a significant impact on the maximum velocity of the SJ. Independent of the orifice shape, the maximum velocity increased with the decrease of the dimensionless stroke length. The higher dimensionless stroke length for the same characteristic velocity and the same characteristic length scale (see Equation (6)) is realized with decreasing frequency of the actuator and thus the higher peak-to-peak deflection of the loudspeaker diaphragm [38,39]. The dimensionless stroke length can be identified as the ratio of the length at which the air was pushed out from the actuator cavity and the diameter of the orifice and governs the distance of the vortex ring moving away from the jet exit [18]. The centerline dimensionless time-averaged velocity was higher near the orifice at $L_0 = 2$ than at $L_0 = 10$, but it decreased faster with the distance from the orifice. The dimensionless time-averaged velocity profile at the distance $x/d = 10$ and $L_0 = 2$ and 10 are presented in Figures 9 and 10 respectively. For the SJ radial velocity profiles at the axial distance equal to $x/d = 10$, the distributions for various orifice shapes are similar to Gaussian profile. For $L_0 = 2$, the U_c/U_e was equal to 0.58 for the circular and square orifices and equal to 0.50 for the slot, while at $L_0 = 10$, for all radial velocity profiles, the ratio of U_c/U_e was equal to 0.71.

3.2. The Turbulent Kinetic Energy of the Synthetic Jet

The dimensionless TKE fields of the SJ at $Re = 5000$ and $L_0 = 2$ and 10 are presented in Figures 11 and 12. The TKE for the circle orifice is presented in Figures 11a and 12a; for the square orifice, it is presented in Figures 11b and 12b; and for the slot orifice, in Figure 11d,e and Figure 12d,e. Additionally, the centerline distributions of the dimensionless TKE are presented in Figures 13 and 14 for $L_0 = 2$ and 10, respectively. The TKE radial distributions at $x/d = 10$ are presented in Figures 15 and 16.

3.2.1. Impact of the Orifice Shape on the Turbulent Kinetic Energy

The dimensionless TKE at $L_0 = 2$ had the highest value near the orifice, and at the distance $2 < x/d < 6$, it had the highest value around the centerline. This shape of the TKE field can be compared to the shape of rabbit ears. The highest values of dimensionless TKE were observed in the case of the slot orifice (Figure 11c) and then in the case of the square orifice (Figure 11b), and the lowest in the case of the circle orifice (Figure 11a). The TKE field decreased with the increased the distance, x/d ; the fastest decreasing rate was for the slot orifice, and the lowest decreasing rate is for square orifice. Similar dependence can be observed in Figure 12 at $L_0 = 10$. The dimensionless TKE centerline distributions (Figures 13 and 14) showed that the TKE for the square orifice was higher than for the circle orifice at the distance $x/d < 4$. The TKE for the slot orifice was higher than for the square at a distance of $0.5 < x/d < 3$ at $L_0 = 2$ (Figure 13) and at a distance of $2.4 < x/d < 3.4$ at $L_0 = 10$ (Figure 14). The initial decline and subsequent increase in TKE in the case of the circle and square orifice at $L_0 = 2$ visible in Figure 13 were also observed by Crispio et al. [17] for the SJA with the chevron and circle nozzle and was named a calming effect by Zaman et al. [40], who observed this effect for the continuous jet. This effect was not observed in the case of the slot SJ and at $L_0 = 10$.

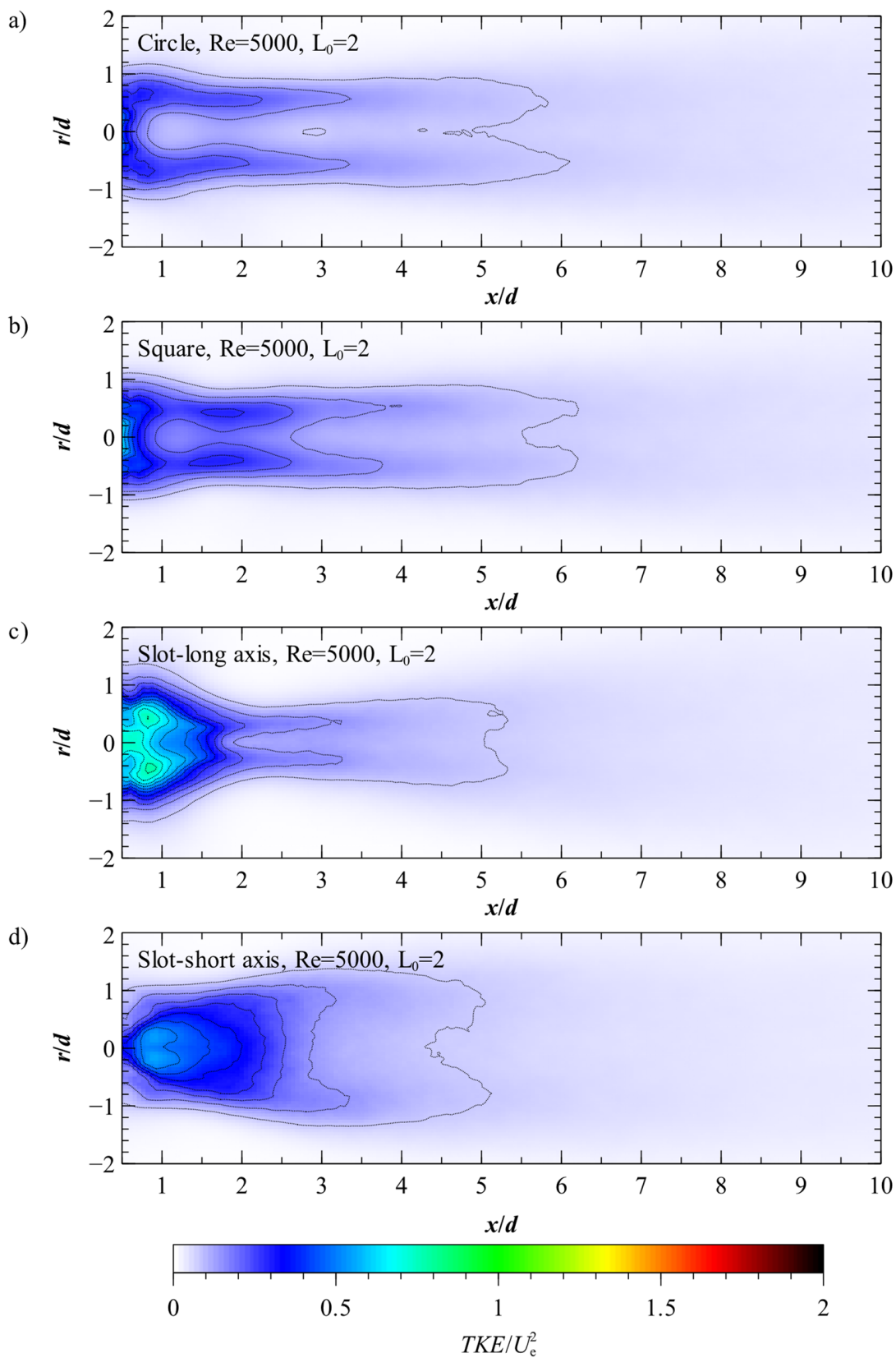


Figure 11. Synthetic jet dimensionless turbulent kinetic energy field at $Re = 5000$, $St = 0.5$, and $L_0 = 2$: (a) circle orifice, (b) square orifice, (c) slot-long side, and (d) slot-short side.

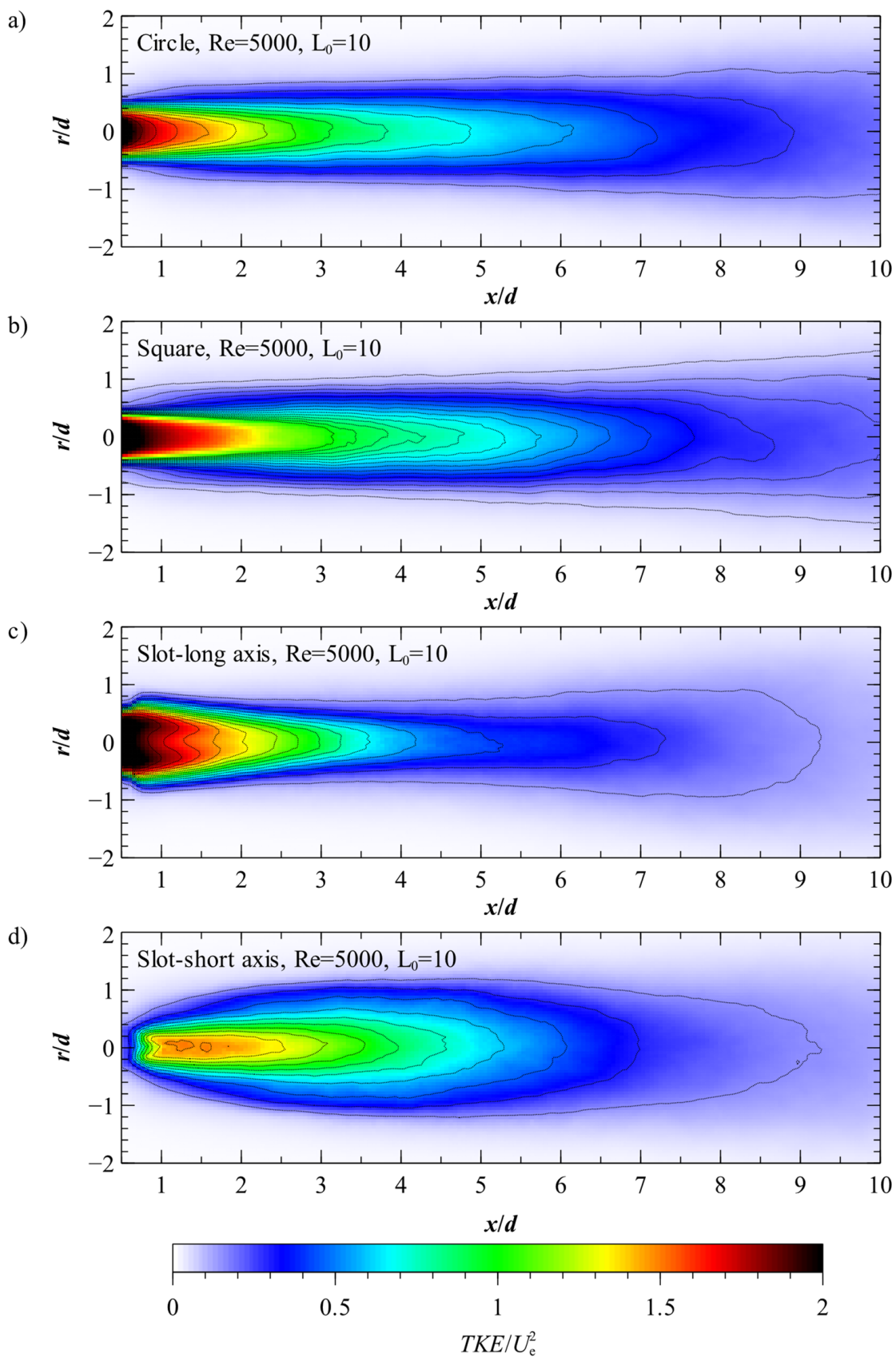


Figure 12. Synthetic jet dimensionless turbulent kinetic energy field at $Re = 5000$, $St = 0.1$, and $L_0 = 10$: (a) circle orifice, (b) square orifice, (c) slot-long side, and (d) slot-short side.

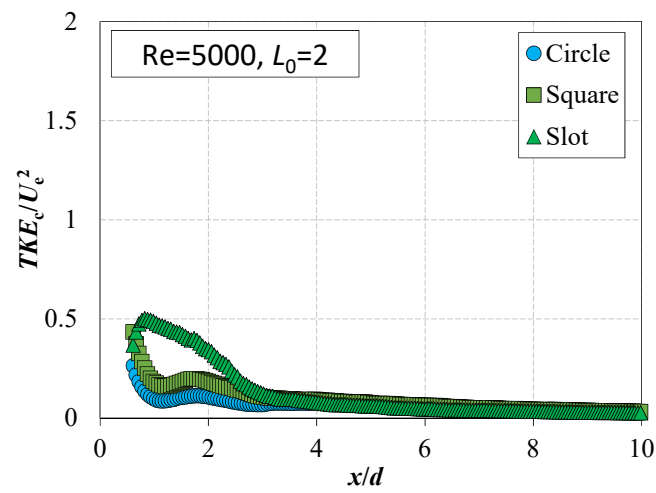


Figure 13. Centerline dimensionless turbulent kinetic energy axial distribution at $L_0 = 2$.

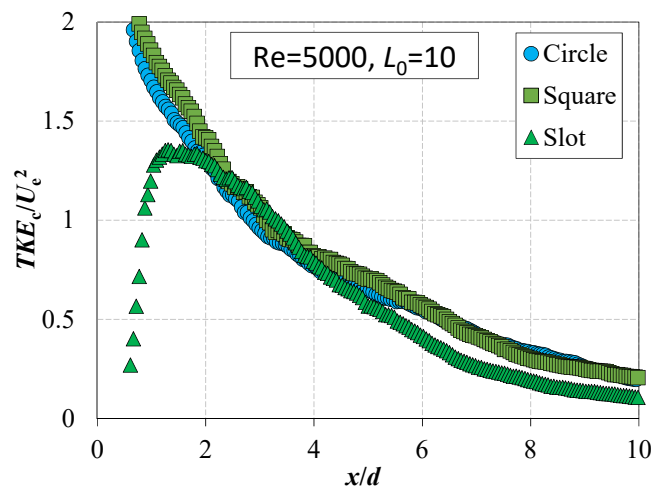


Figure 14. Centerline dimensionless turbulent kinetic energy axial distribution at $L_0 = 10$.

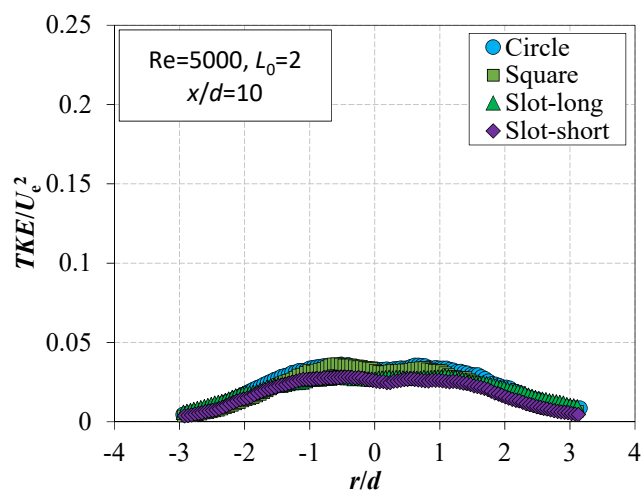


Figure 15. Dimensionless turbulent kinetic energy radial distribution at $L_0 = 2$.

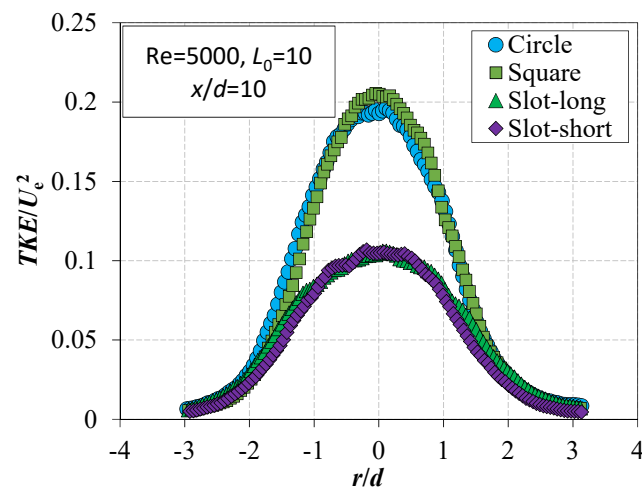


Figure 16. Dimensionless turbulent kinetic energy radial distribution at $L_0 = 10$.

As mentioned, the TKE field width for the slot SJ contract for the slot-long side and expand for the slot-short side. This behavior complies with the flow structure of the slot SJ [14]. The higher SJ TKE level in the case of the slot orifice concerning the circle orifice was demonstrated by Miró et al. [20]. They observed that the slot SJ lost its coherent structure and thus produced a higher level of TKE. Therefore, the square and slot SJ enhanced the heat transfer better than the circle SJ [21,22], and this can be related to the higher TKE. The highest Nusselt number for the impingement SJ was achieved for a distance of $x/d < 5$ for slot orifice and $x/d > 5$. Moreover, it should be remembered that the efficiency of the SJ in cooling applications depends also on the dimensionless stroke length [2]. This is in line with the presented results.

3.2.2. Impact of the Dimensionless Stroke Length on the Turbulent Kinetic Energy

The value of the dimensionless stroke length has a significant impact on the TKE value and distribution. The specific structure of the rabbit ears was observed only in the case of $L_0 = 2$ (Figure 11), and it disappeared at $L_0 = 10$ (Figure 12). The radial profile of TKE showed that this specific structure of the TKE field was visible also at the distance of $x/d = 10$, where the maximum value of the TKE was measured near the axis at $L_0 = 2$ (at $r/d = 0.5$ or -0.5 ; see Figure 15) and in the axis at $L_0 = 10$ (Figure 16). Thus, at the small value of dimensionless stroke length, the highest value of the TKE was observed for the region of the vortex ring, and with the increasing stroke length, the turbulence in the axis of the vortex ring increased. The width of the TKE field at $L_0 = 2$ decreased at the distance $x/d > 1$.

The five-times increase of the dimensionless stroke length from $L_0 = 2$ to $L_0 = 10$ increased the TKE significantly, almost three times in the case of the slot orifice and over five times in the case of the circle and square orifices at the distance $x/d = 10$ (Figures 13 and 14).

3.3. The Time-Averaged Vorticity Field of the Synthetic Jet

The vorticity field of SJ is presented in Figures 17 and 18 at $Re = 5000$ and $L_0 = 2$ and 10, respectively. The positive value of the vorticity field means the rotation to the left side, and the negative value of the vorticity means the rotation to the right side. Additionally, the radial vorticity profile of the SJ is presented in Figures 19 and 20 at the distance of $x/d = 10$.

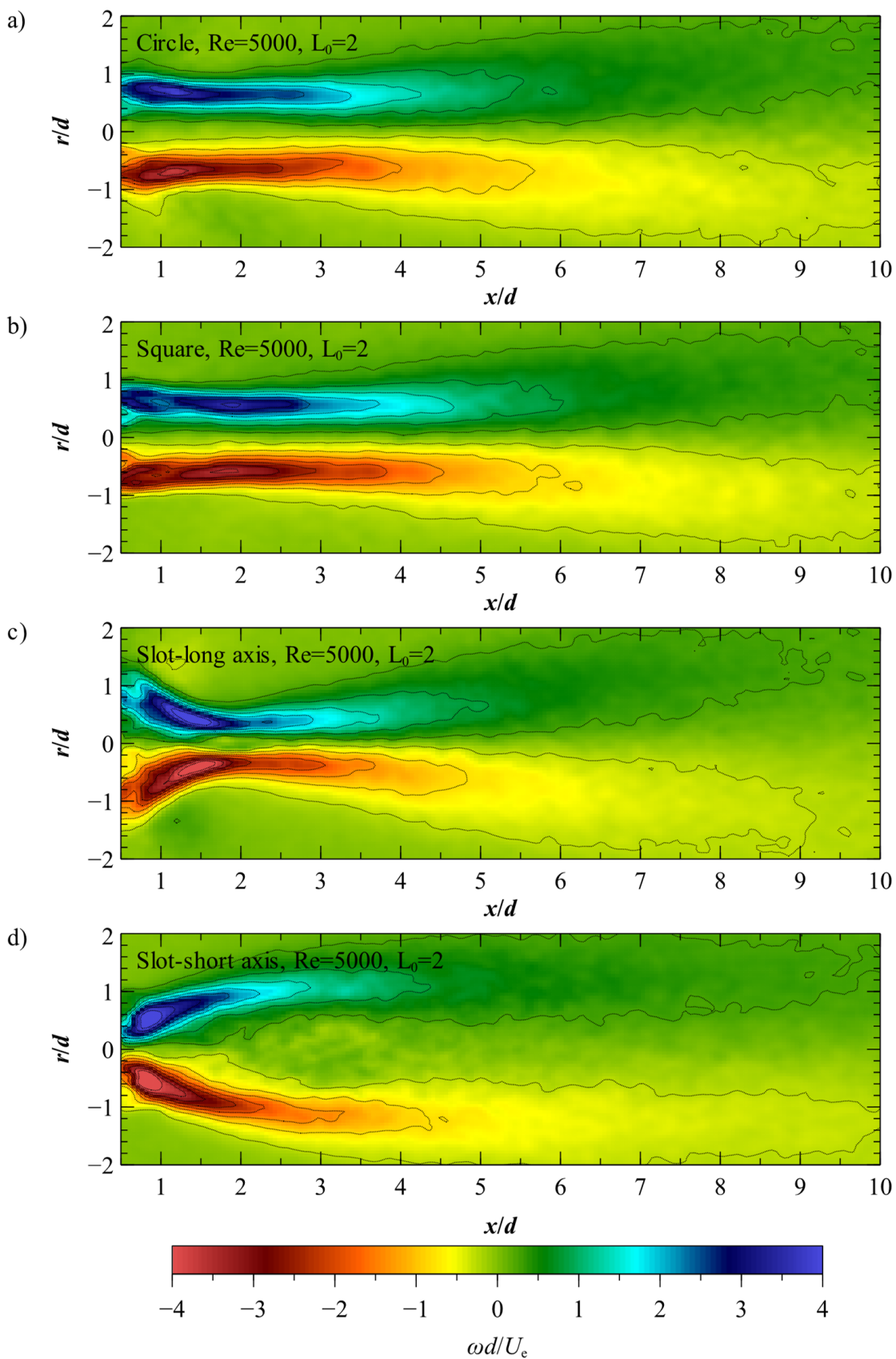


Figure 17. Synthetic jet dimensionless vorticity field at $Re = 5000$, $St = 0.5$, and $L_0 = 2$: (a) circle orifice, (b) square orifice, (c) slot-long side, and (d) slot-short side.

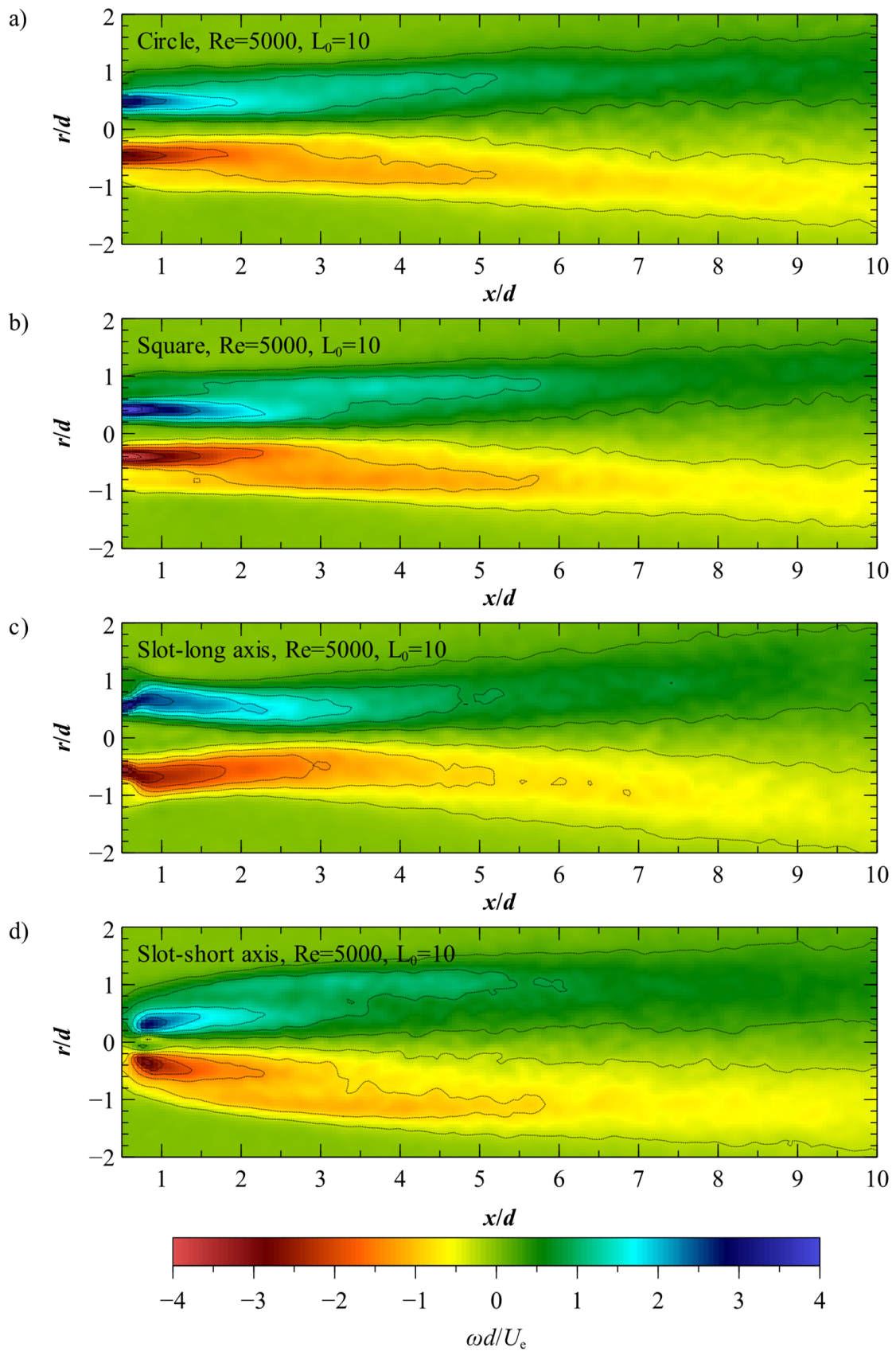


Figure 18. Synthetic jet dimensionless vorticity field at $Re = 5000$, $St = 0.1$, and $L_0 = 10$: (a) circle orifice, (b) square orifice, (c) slot-long side, and (d) slot-short side.

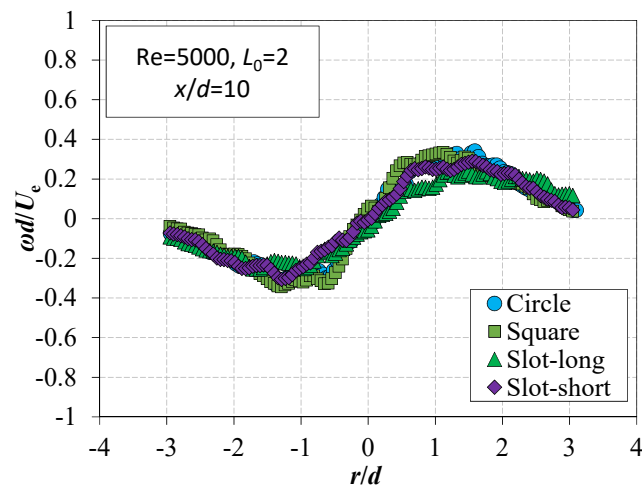


Figure 19. Dimensionless vorticity radial distribution at $L_0 = 2$.

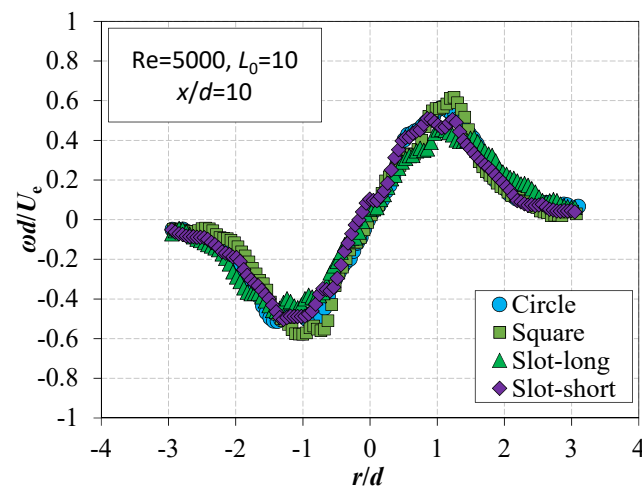


Figure 20. Dimensionless vorticity radial distribution at $L_0 = 10$.

3.3.1. Impact of the Orifice Shape on the Vorticity

The time-averaged vorticity field of the SJ observed in Figures 17 and 18 for the circle and square orifices (a and b) was typical. In the figures, we observed two axisymmetric fields with opposite values. These fields correspond to the areas at which the vortices propagate. The SJ coherent structure produces a high vorticity field. At the centerline, the time-averaged vorticity is equal to zero. The vortex ring had a similar shape to the circle and square orifices [12] in the axis on which the measurement was carried out (Figure 2). The difference in flow topology for the circle and square SJ is visible during the diagonal measurement, but these measurements were not carried out in the present study. The dimensionless vorticity was equal to or lower than 1 at a distance around $x/d = 6$ for the circle and square SJs (Figure 17a,b and Figure 18a,b). Thus, it can be concluded that the coherent structure of the SJ was lost at this distance, but it did not mean the disappearance of vortices. The radial vorticity profile at a distance of $x/d = 10$ (Figures 19 and 20) showed that the maximal value of the dimensionless vorticity was equal to 0.3 (Figure 19, $L_0 = 2$) and 0.6 (Figure 20, $L_0 = 10$). The decrease in vorticity can be caused by the vortex ring coalescing caused by a high Reynolds number, which has already been observed by Carter and Soria [15]. They did not observe the ring coalescing at $Re = 7784$ and $St = 0.012$. The investigated SJ had a lower Reynolds number but a higher Strouhal number, which also has a significant impact on topologies on the SJ. The effect of the coalescing of vortex rings at a certain distance from the orifice has also been observed by Dančová et al. [25] at $Re = 199$ and $St = 0.22$.

The time-averaged vorticity field of the slot SJ contracts for the slot-long side at the distance $1 < x/d < 2$ (Figures 17c and 18c) and expands along the slot-short side. The vorticity field expands significantly from the orifice outlet to the distance $x/d = 4$ (Figures 17d and 18d). This shape of the vorticity field is coherent with the evolution of the slot SJ presented by Wang et al. [12].

3.3.2. Impact of the Dimensionless Stroke Length on the Time-Averaged Vorticity Field

The SJ vorticity field at $L_0 = 10$ had a lower dissipation rate than the vorticity at $L_0 = 2$. It is especially visible in Figures 19 and 20, where the radial vorticity profiles at a distance of $x/d = 10$ were presented. The maximal value of dimensionless vorticity at $L_0 = 2$ was approximately equal to 0.35, and at $L_0 = 10$, it was approximately equal to 0.6. It indicates the slower disappearance of the vortex structure. However, the vorticity at a low distance from the orifice $x/d < 4$ was higher at $L_0 = 2$, and a field area of very high vorticity ($\omega d/U_e > |3.5|$) was also higher at $L_0 = 2$. The faster disappearance of the vortex ring is caused by the higher value of the normal stress. Xu and Wang [11] showed that the increased dimensionless stroke length caused a decrease in the time-averaged normal stress near the orifice.

As was mentioned in Section 3.3.1, the decrease in vorticity can be identified with the vortex ring coalescing. This is indicated by the visualizations carried out by Carter and Soria [15] and Dančová et al. [25]. Trávníček et al. [41] visualized the SJ at $L_0 = 3.29; 2.33; 1.75$ and $Re = 17,000; 12,000; 9000$, respectively. The vortex ring coalescing was not observed only at $L_0 = 3.29$ and $Re = 17,000$. The SJ coalesced at a distance of $x/d = 4$ and 3 at $L_0 = 2.33$ and 1.75, respectively. On the other hand, Dančová et al. [25] observed the vortex ring coalescing at $Re = 199$ and $St = 0.22$ ($L_0 = 4.55$) and at a distance of approximately $x/d = 3$, and Carter and Soria [15] at $Re = 7784$ and $St = 0.012$ ($L_0 = 83.3$). Wang et al. [12] did not recognize the distance and parameter at which the vortex ring coalescing occurred. However, the slot SJ visualization presented in their article showed that the SJ coalesced at a distance of $x/d = 4$ at $Re \geq 332$ and $L_0 = 2.3$. Ghaffari et al. [23] did not observe the vortex ring coalescing at $Re = 890; 900$ and $L_0 = 2.2; 10$, respectively.

A visualization made by Xu and Wang [11] showed that the value of phase-averaged dimensionless vorticity below 0.5 results in the loss of the SJ's coherent structure. However, Ghaffari et al. [23] showed that the coherent structure of the SJ can be preserved even for the value of a time-averaged dimensionless vorticity field equal to approximately 0.25 for the SJ at $Re = 900$ and $L_0 = 10$.

4. Conclusions

In this study, the circle, square, and slot orifices were investigated at the same Reynolds number, i.e., $Re = 5000$, and two different dimensionless stroke lengths, i.e., $L_0 = 2$ and 10. The orifices had the same equivalent diameter. The flow fields of time-averaged velocity, TKE, and vorticity were determined based on the PIV measurements. Additionally, the axial and radial profiles at a distance of $x/d = 10$ were presented. It is a very large data set that is unique and has not been comprehensively presented in any of the analyzed works from the literature. The data should be used to validate the numerical measurements.

The maximum value of the time-averaged velocity decreased with the increase of the dimensionless stroke length. However, the time-averaged velocity decreased more slowly at $L_0 = 10$, and as a result, it was higher at a distance of $x/d = 10$ than the time-averaged velocity at $L_0 = 2$ and the same distance. Nevertheless, the TKE was much higher at $L_0 = 10$ than at $L_0 = 2$. In the case of the circle and square orifices, the centerline distributions of the velocity and TKE decreased slower than in the case of slot orifices. The flow fields of the time-averaged velocity, TKE, and vorticity for the slot-long side contract at some distance from the orifice and then later expand.

The dimensionless vorticity at a low distance from the orifice $x/d < 4$ was higher at the $L_0 = 2$, and a field area of very high vorticity ($\omega d/U_e > |3.5|$) was also higher at $L_0 = 2$. The low dimensionless stroke length at the same Reynolds number appears for

higher actuation frequency (see Table 1). It is less time between the next expulsions of fluid, in which the SJ can be formed, and the loudspeaker membrane peak-to-peak distance must be slighter. The flow is more orderly, and the TKE is lower than for the high dimensionless stroke length, despite the higher velocity. For the same reason, the parameters of the SJ decreased faster at $L_0 = 2$ than at $L_0 = 10$.

Author Contributions: Conceptualization, E.S. and P.G.; methodology, E.S., P.G. and P.D.; software, P.G.; validation, P.G.; formal analysis, E.S. and P.G.; investigation, E.S. and P.G.; resources, P.G.; data curation, E.S.; writing—original draft preparation, E.S.; writing—review and editing, M.J., P.G. and P.D.; visualization, E.S. and P.G.; supervision, P.G. and P.D.; project administration, P.G.; funding acquisition, P.G. All authors have read and agreed to the published version of the manuscript.

Funding: This work was supported by the National Center for Research and Development, Poland, Grant No. LIDER/6/0024/L-10/18/NCBR/2019.

Institutional Review Board Statement: Not applicable.

Informed Consent Statement: Not applicable.

Data Availability Statement: All data generated or used during the study are available from the corresponding author upon request.

Conflicts of Interest: The authors declare no conflict of interest.

Nomenclature

a, b	orifice width (mm)
d	orifice equivalent diameter (mm)
D	diameter of effective area of loudspeaker (mm)
f	signal frequency (Hz)
f_{PIV}	PIV sampling frequency (Hz)
A	orifice cross-section area (mm ²)
U_c	centerline velocity (m/s)
U_e	characteristic velocity (m/s)
U	time-averaged velocity in x-direction (m/s)
V	time-averaged velocity in r-direction (m/s)
Re	Reynolds number (-)
L_0	dimensionless stroke length (-)
T	oscillation period (s)
TKE	turbulent kinetic energy (m ² /s ²)
ω	vorticity (1/s)
r	radial coordinate (mm)
x	axial coordinate (mm)
m	mass (kg)
n	number of the membrane oscillation period
g	gravitation acceleration (m/s ²)
u	instantaneous velocity in x-direction (m/s)
v	instantaneous velocity in r-direction (m/s)
ν	kinematic viscosity (m ² /s)
τ	time (s)
ρ	air density (kg/m ³)
N	number of measurements
N_{DIV}	number of the phases sampled during PIV measurements

References

1. Gil, P. Experimental investigation on heat transfer enhancement of air-cooled heat sink using multiple synthetic jets. *Int. J. Therm. Sci.* **2021**, *166*, 106949. [[CrossRef](#)]
2. Singh, P.K.; Shah, A.K.; Tripathi, S.N.; Yadav, H.; Upadhyay, P.K.; Sahu, S.K. Numerical investigation of the flow and thermal behavior of impinging single and multi-orifice synthetic jets with different waveforms. *Numer. Heat Transf. Part A Appl.* **2022**, *82*, 1–21. [[CrossRef](#)]

3. De Giorgi, M.G.; De Luca, C.G.; Ficarella, A.; Marra, F. Comparison between synthetic jets and continuous jets for active flow control: Application on a NACA 0015 and a compressor stator cascade. *Aerosp. Sci. Technol.* **2015**, *43*, 256–280. [[CrossRef](#)]
4. Liang, Y.; Taya, M.; Xiao, J.Q.; Xiao, G. Design of an inchworm actuator based on a ferromagnetic shape memory alloy composite. *Smart Mater. Struct.* **2012**, *21*, 115005. [[CrossRef](#)]
5. Al-Atabi, M. Experimental Investigation of the Use of Synthetic Jets for Mixing in Vessels. *J. Fluids Eng.* **2011**, *133*, 094503. [[CrossRef](#)]
6. Dvořák, V.; Dančová, P.; Švarc, P. Experimental investigation into flow in an ejector with four synthetic jets. *EPJ Web. Conf.* **2012**, *25*, 02003. [[CrossRef](#)]
7. Rimasauskienė, R.; Matejka, M.; Ostachowicz, W.; Kurowski, M.; Malinowski, P.; Wandowski, T.; Rimasauskas, M. Experimental research of the synthetic jet generator designs based on actuation of diaphragm with piezoelectric actuator. *Mech. Syst. Signal Process.* **2015**, *50–51*, 607–614. [[CrossRef](#)]
8. Ikhtlaq, M.; Yasir, M.; Ghaffari, O.; Arik, M. Acoustics and Heat Transfer Characteristics of Piezoelectric Driven Central Orifice Synthetic Jet Actuators. *Exp. Heat Transf.* **2021**, *35*, 758–779. [[CrossRef](#)]
9. Jankee, G.K.; Ganapathisubramani, B. Scalings for rectangular synthetic jet trajectory in a turbulent boundary layer. *J. Fluid Mech.* **2021**, *915*, A57. [[CrossRef](#)]
10. Ben Chiekh, M.; Ferchichi, M.; Michard, M.; Guellouz, M.S.; Béra, J.-C. Synthetic jet actuation strategies for momentumless trailing edge wake. *J. Wind Eng. Ind. Aerodyn.* **2013**, *113*, 59–70. [[CrossRef](#)]
11. Xu, Y.; Wang, J.J. Digital particle image velocimetry study on parameter influence on the behavior of impinging synthetic jets. *Exp. Therm. Fluid Sci.* **2019**, *100*, 11–32. [[CrossRef](#)]
12. Wang, L.; Feng, L.-H.; Wang, J.-J.; Li, T. Parameter influence on the evolution of low-aspect-ratio rectangular synthetic jets. *J. Vis.* **2018**, *21*, 105–115. [[CrossRef](#)]
13. Neal, D.R.; Sciacchitano, A.; Smith, B.L.; Scarano, F. Collaborative framework for PIV uncertainty quantification: The experimental database. *Meas. Sci. Technol.* **2015**, *26*, 074003. [[CrossRef](#)]
14. Smith, B.L.; Glezer, A. The formation and evolution of synthetic jets. *Phys. Fluids* **1998**, *10*, 2281–2297. [[CrossRef](#)]
15. Carter, J.E.; Soria, J. The evolution of round zero-net-mass-flux jets. *J. Fluid Mech.* **2002**, *472*, 167–200. [[CrossRef](#)]
16. Violato, D.; Scarano, F. Three-dimensional evolution of flow structures in transitional circular and chevron jets. *Phys. Fluids* **2011**, *23*, 124104. [[CrossRef](#)]
17. Crispo, C.M.; Greco, C.S.; Avallone, F.; Cardone, G. On the flow organization of a chevron synthetic jet. *Exp. Therm. Fluid Sci.* **2017**, *82*, 136–146. [[CrossRef](#)]
18. Shuster, J.M.; Smith, D.R. Experimental study of the formation and scaling of a round synthetic jet. *Phys. Fluids* **2007**, *19*, 045109. [[CrossRef](#)]
19. Holman, R.; Utturkar, Y.; Mittal, R.; Smith, B.L.; Cattafesta, L. Formation criterion for synthetic jets. *AIAA J.* **2005**, *43*, 2110–2116. [[CrossRef](#)]
20. Miró, A.; Soria, M.; Cajas, J.C.; Rodríguez, I.; Moulinec, C. Flow topology and heat transfer analysis of slotted and axisymmetric synthetic impinging jets. *Int. J. Therm. Sci.* **2021**, *164*, 106847. [[CrossRef](#)]
21. Chaudhari, M.; Puranik, B.; Agrawal, A. Effect of orifice shape in synthetic jet based impingement cooling. *Exp. Therm. Fluid Sci.* **2010**, *34*, 246–256. [[CrossRef](#)]
22. Singh, P.K.; Sahu, S.K.; Upadhyay, P.K.; Jain, A.K. Experimental investigation on thermal characteristics of hot surface by synthetic jet impingement. *Appl. Therm. Eng.* **2020**, *165*, 114596. [[CrossRef](#)]
23. Ghaffari, O.; Solovitz, S.A.; Arik, M. An investigation into flow and heat transfer for a slot impinging synthetic jet. *Int. J. Heat Mass Transf.* **2016**, *100*, 634–645. [[CrossRef](#)]
24. Zhao, Z.; Ding, J.; Shi, S.; Kaufmann, R.; Ganapathisubramani, B. Volumetric flow characterisation of a rectangular orifice impinging synthetic jet with single-camera light-field PIV. *Exp. Therm. Fluid Sci.* **2021**, *123*, 110327. [[CrossRef](#)]
25. Dančová, P.; Trávníček, Z.; Vít, T. Experimental investigation of a synthetic jet array in a laminar channel flow. *EPJ Web Conf.* **2013**, *45*, 01002. [[CrossRef](#)]
26. Smyk, E.; Wilk, J.; Markowicz, M. Synthetic Jet Actuators with the Same Cross-Sectional Area Orifices-Flow and Acoustic Aspects. *Appl. Sci.* **2021**, *11*, 4600. [[CrossRef](#)]
27. Gil, P. Synthetic jet Reynolds number based on reaction force measurement. *J. Fluids Struct.* **2018**, *81*, 466–478. [[CrossRef](#)]
28. Kordík, J.; Trávníček, Z. Optimal diameter of nozzles of synthetic jet actuators based on electrodynamic transducers. *Exp. Therm. Fluid Sci.* **2017**, *86*, 281–294. [[CrossRef](#)]
29. Xue, Z.; Charonko, J.J.; Vlachos, P.P. Particle image velocimetry correlation signal-to-noise ratio metrics and measurement uncertainty quantification. *Meas. Sci. Technol.* **2014**, *25*, 115301. [[CrossRef](#)]
30. Greco, C.S.; Ianiro, A.; Astarita, T.; Cardone, G. On the near field of single and twin circular synthetic air jets. *Int. J. Heat Fluid Flow* **2013**, *44*, 41–52. [[CrossRef](#)]
31. Trávníček, Z.; Tesař, V. Annular impinging jet with recirculation zone expanded by acoustic excitation. *Int. J. Heat Mass Transf.* **2004**, *47*, 2329–2341. [[CrossRef](#)]
32. Gil, P.; Smyk, E. Synthetic jet actuator efficiency based on the reaction force measurement. *Sens. Actuators A Phys.* **2019**, *295*, 405–413. [[CrossRef](#)]

33. Kordík, J.; Trávníček, Z. Integral Quantities of Axisymmetric Synthetic Jets Evaluated from a Direct Jet Thrust Measurement. *Flow Turbul. Combust.* **2019**, *103*, 827–844. [[CrossRef](#)]
34. Antošov, Z.; Trávníček, Z. Control of a Round Jet Intermittency and Transition to Turbulence by Means of an Annular Synthetic Jet. *Actuators* **2021**, *10*, 185. [[CrossRef](#)]
35. Tan, X.; Zhang, J.; Yong, S.; Xie, G. An experimental investigation on comparison of synthetic and continuous jets impingement heat transfer. *Int. J. Heat Mass Transf.* **2015**, *90*, 227–238. [[CrossRef](#)]
36. Smith, B.L.; Swift, G.W. A comparison between synthetic jets and continuous jets. *Exp. Fluids* **2003**, *34*, 467–472. [[CrossRef](#)]
37. Zong, H.; Kotsonis, M. Effect of slotted exit orifice on performance of plasma synthetic jet actuator. *Exp. Fluids* **2017**, *58*, 17. [[CrossRef](#)]
38. Mohseni, K.; Mittal, R. *Synthetic Jets: Fundamentals and Applications*; Mohseni, K., Mittal, R., Eds.; CRC Press: Boca Raton, FL, USA, 2014; ISBN 978-1-4398-6810-2.
39. Krishnan, G.; Mohseni, K. An Experimental and Analytical Investigation of Rectangular Synthetic Jets. *J. Fluids Eng.* **2009**, *131*, 121101. [[CrossRef](#)]
40. Zaman, K.; Bridges, J.; Huff, D. Evolution from ‘tabs’ to ‘chevron technology’—A review. *Noise Notes* **2012**, *11*, 27–48. [[CrossRef](#)]
41. Trávníček, Z.; Broucková, Z.; Kordík, J. Formation criterion for axisymmetric synthetic jets at high stokes numbers. *AIAA J.* **2012**, *50*, 2012–2017. [[CrossRef](#)]

Disclaimer/Publisher’s Note: The statements, opinions and data contained in all publications are solely those of the individual author(s) and contributor(s) and not of MDPI and/or the editor(s). MDPI and/or the editor(s) disclaim responsibility for any injury to people or property resulting from any ideas, methods, instructions or products referred to in the content.